2

Deformation Structures and Recrystallization in Magnesium Alloys

Étienne Martin[1], Raj K. Mishra[2] and John J. Jonas[1]
[1]*McGill University, Montreal, QC, H3A 2B2,*
[2]*General Motors Research and Development Center, Warren, MI, 48090,*
[1]*Canada*
[2]*USA*

1. Introduction

Magnesium, being a hexagonal close-packed metal, has limited ductility and poor formability at room temperature. These characteristics hinder the production of magnesium wrought products, which represent a mere 1% of the total annual magnesium usage (Polmear, 1995). Formability can be significantly increased when additional slip systems are thermally activated. As such, hot deformation is extensively used to produce wrought magnesium products such as sheet metal or extruded bars and tubes (Barnett, 2001). Besides ductility limitations, Mg alloys also suffer from strong mechanical anisotropy (Kleiner & Uggowitzer, 2004). Depending on the crystallographic texture, different combinations of deformation systems may be activated. Since the deformation modes available for displacements parallel to the c-axis are limited, the crystallographic orientation has a strong influence on the deformation of Mg.

In many metals, dynamic recrystallization leads to the randomization of initial textures and can therefore be of practical interest with regards to subsequent forming (Humphreys & Hatherly, 2004). According to the literature, recrystallization is not usually accompanied by sharp changes in the crystallographic texture. Yi et al. (Yi et al., 2006) have reported, for example, that the ODF (orientation distribution function) intensities in AZ31 were similar in the large deformed and small dynamically recrystallized (DRX) grains. (Nevertheless, they did observe a slight shift in the location of the main texture component.) Other investigators have reported that most of the newly recrystallised grains in Mg alloys have orientations similar to those of the matrix grains, but with slightly weaker intensities (Backx et al., 2004; del Valle et al., 2005; Jäger et al., 2006). Such recrystallization appears to promote 30^{o} <0001> rotations that preserve the basal texture or, at the very least, delay its decomposition (Gottstein & Al Samman, 2005; Beausir et al., 2007). However, these investigations were mostly performed on highly deformed samples, so that it is difficult to separate the influence of the different recrystallization and deformation mechanisms on the texture.

In magnesium, basal glide invariably leads to a basal texture (i.e. c-axis aligned with the compression axis (CA)) or perpendicular to the tensile axis (TA)). However, different twinning and slip systems can also be activated under different deformation conditions (i.e. temperature, strain rate, texture, etc.). It is well known that the deformed state has a strong influence on recrystallization, and several studies have linked the different deformation

structures found in magnesium to the recrystallization behavior (Ion et al., 1982; Galiyev et al., 2001; Myshlyaev et al., 2002). However, few have mentioned its effects on the texture, and most studies to date have focused on relatively small orientation scan areas. Thus, while these studies provide some insight, it should be noted that the number of grains and grain boundaries sampled are not statistically reliable. While presenting a more statistically relevant picture of these phenomena, this chapter aims to characterize the orientation aspects of deformation structures and to follow their evolution during recrystallization.

2. Misorientations and Rodrigues-Frank space

It is essential to note that slip and twinning take place by simple shear and not pure shear: they correspond to a displacement in the shear direction on one side of the shear plane (Kocks et al., 1998). Since the occurrence of simple shear induces rotations, it is appropriate to characterize the deformation structures in terms of the misorientations that are produced with respect to their neighborhoods. There are different ways of representing a misorientation between two given crystallographic orientations (Mason & Schuh, 2008). The angle and axis pair (ω, d) is a convenient method as it involves readily recognizable geometric quantities and enables the physical effect of the rotation to be visualized in a straightforward manner. For this purpose, the orientation matrices identifying crystallites A and B in the specimen coordinate system are labeled $\mathbf{g_A}$ and $\mathbf{g_B}$, respectively. Here, $\mathbf{g}$ defines a rotation that brings the laboratory coordinate system into coincidence with that of a crystallite. Then, the misorientation matrix M_{AB} relating two crystallites, where crystallite A is arbitrarily chosen to be the reference system, is given by (Engler & Randle, 2010):

$$M_{AB}=g_B g_A^{-1}. \tag{1}$$

This matrix defines a rotation that converts the coordinate system of the reference crystallite into that of the other crystallite. The angle-axis pair associated with M_{AB} is then defined as

$$\omega = \arccos(\frac{1}{2}[\mathrm{trace}(M_{AB})-1]) \tag{2}$$

$$[d_1,d_2,d_3] =[m_{23}-m_{32},\ m_{31}-m_{13},\ m_{12}-m_{21}] \tag{3}$$

Here $\boldsymbol{\omega}$ is the misorientation angle between crystallites A and B, d_i (i=1,2,3) are the axial components of the rotation axis d, and m_{ij} (i,j=1,2,3) are the elements of M_{AB}. Note that the minimum angle-axis pair representation is used here; it is obtained by taking the crystal symmetry into account (Engler & Randle, 2010).

The angle-axis pair can be represented in three dimensions by combining the unit vector $\mathbf{d}$ and the rotation angle $\boldsymbol{\omega}$ using the Rodrigues formula (Frank, 1988) given by:

$$R =\tan\frac{\omega}{2}[d_1,\ d_2,\ d_3] \tag{4}$$

Each misorientation can then be described by the three components (R_1,R_2,R_3) of the Rodrigues-Frank vector. When the minimum angle-axis pair representation is employed, Rodrigues-Frank space is reduced to a finite subspace called the fundamental zone, which can be further reduced by considering only 1/24 of this space (Heinz & Neumann, 1991) in the case of hexagonal materials.

3. Initial material

The present work is based on investigations that were carried out on extruded tubes of magnesium alloys AM30 and AZ31 (Martin et al., 2009; Martin et al., 2010; Martin & Jonas, 2010). The tubes from which the samples were made were extruded using porthole dies. The chemical compositions of the two materials are presented in Table 1. The most significant difference between the two alloys is their zinc (Zn) content: the amount of Zn in AM30 is considerably lower than in AZ31.

	Al	Zn	Mn	Fe	Ni	Cu
AZ31	3.1	1.05	0.54	0.0035	0.007	0.008
AM30	3.4	0.16	0.33	0.0026	0.006	0.008

Table 1. Chemical compositions of the AZ31 and AM30 alloy samples (in wt. %).

The initial grain orientations of the as-received tubes consist of two main components: one with its *c*-axis approximately parallel to the radial direction (called the RD or $\{10\bar{1}0\}<1\bar{2}10>$ component) and the other with its *c*-axis approximately parallel to the tangential direction (called the TD or $\{1\bar{2}10\}<0001>$). The above planes are normal to the extrusion direction (ED) and the directions parallel to TD.

The macrotextures of the as-received tubes are shown in Fig. 1. in the form of inverse pole figures. The volume fractions of the two components were similar in the AM30 (48 % for the TD and 39 % for the RD), while the AZ31 had a stronger TD component (65 %) compared to the RD (15 %) (Jiang et al., 2007). A fibre texture links the two components by continuous rotations around $\boldsymbol{\Phi}$ of ± 90° and $\boldsymbol{\varphi_2}$ of ± 30° starting from the TD orientation (0,0,30) and ending at the RD orientation (0,90,0) (following the Bunge notation (Bunge, 1982)).

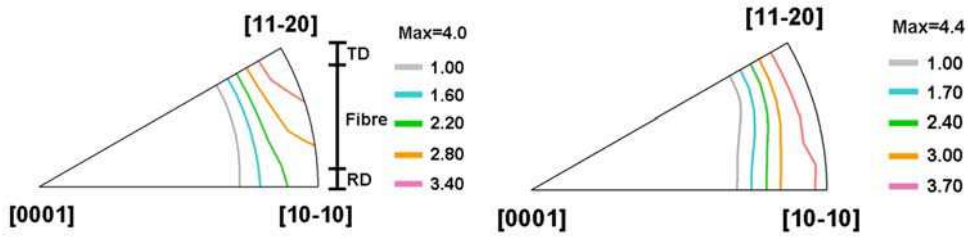

(a) (b)

Fig. 1. Inverse pole figures that display the orientation of the extrusion direction in the hexagonal crystal reference frame of the (a) AZ31 and (b) AM30.

4. Recrystallization of twins

Above the critical value of the Zener–Hollomon parameter for the activation of twinning (~ 7×10^{12} s^{-1}), the deformation of magnesium takes place by both slip and twinning (Barnett, 2003). Two types of twins are frequently reported: i.e. the $\{10\bar{1}2\}$-$<\bar{1}011>$ extension and $\{10\bar{1}1\}$-$<10\bar{1}\bar{2}>$ contraction twins. When elongation along the c-axis is accommodated by the formation of extension twins, the basal planes are reoriented by 86° around a $<1\bar{2}10>$ axis. Such boundaries are very mobile and the extension twins readily

thicken rather than generating further strain localizations (Jiang et al., 2007). Therefore, such twins are not very effective sites for the initiation of recrystallization. Extension twins are essentially activated in the early stages of deformation (when the texture is unstable[1]). As such, they do not have much influence on the final texture during thermomechanical processing, although they accelerate the formation of the deformation (stable) end texture (Godet et al., 2006; Yi et al., 2009b).

By contrast, when contraction along the c-axis is accommodated by the formation of contraction twins, the basal planes are reoriented by 56° around a $< 1\bar{2}10 >$ axis. This change facilitates glide on the basal planes and generates zones of flow localization (Jiang et al., 2006). Because of the polarity of this mechanism, these twins can be activated in grains that have stable orientations. In this way, their formation can modify the previous deformation texture. Moreover, these twins do not thicken significantly, but rather undergo extension twinning in their interiors, also referred to as double twinning (Barnett, 2007). Because of these characteristics, contraction twins can serve as effective sites for recrystallization. In this context, this section will concentrate on the occurrence of recrystallization at contraction and double twins.

In the work described below, the recrystallization of twins was investigated on magnesium samples deformed in tension along the ED. Because the tensile stress was applied along the $< 1\bar{2}10 >$ and $< 01\bar{1}0 >$ directions in the TD and RD components, respectively, or in other words, perpendicular to the c -axis, a deviator stress was induced along the c -axis that is compressive. As a result, the twins induced were of the *contraction* type and also contained double (secondary or extension) twins. In order to maximize the amount of twins generated, the samples were deformed at ambient temperature and a true strain rate of 0.1 s^{-1}. The samples were pulled to true strains 0.15, which is the maximum strain that can be achieved under these conditions. Finally, the twinned samples were annealed at 300 °C for 30 and 60 minutes. The electron backscatter diffraction technique (EBSD) was employed to follow the orientation changes that took place as the recrystallized grains formed within the twins.

4.1 Contraction and double twinning

There are 12 symmetry operations associated with hcp crystals; these lead to the existence of six equivalent contraction and six equivalent extension twin variants. In the case of double twinning, each primary (contraction) twin is associated with six different secondary (extension) twins; these are identified in Table 2. Note that the misorientation relationship associated with each double twin variant in Table 2 is expressed with respect to the *matrix* orientation. The misorientations are therefore not the ones conventionally associated with single extension twins ($< 11\bar{2}0 > 86°$). The current representation reveals that the ensemble of secondary twin variants can be divided into four groups (S^A, S^B, S^C and S^D); here variants C1 and C2 as well as D1 and D2 are subgroups of groups S^C and S^D, respectively. The members of each group are defined by rotations that are geometrically equivalent. Given that there are six different primary twin variants, the S^A and S^B groups each contain 6 variants while the S^C and S^D each contain 12.

[1] Texture stability is defined here with respect to basal glide and the imposed strain path. A crystallographic orientation is stable when the c-axis is aligned with the compression direction or is perpendicular to the tensile axis.

Double twin symmetry group	Double twin symmetry subgroup	Minimum angle-axis pair	Symmetry elements
A	N/A	$<1\bar{2}10>(37.5^o)$	6
B	N/A	$<1\bar{2}10>(30.1^o)$	6
C	C1	$<7\bar{3}\bar{4}2>(66.5^o)$	6
	C2	$<\bar{4}3\bar{7}\bar{2}>(66.5^o)$	6
D	D1	$<14\bar{7}\bar{7}3>(69.9^o)$	6
	D2	$<\bar{7}\bar{7}14\bar{3}>(69.9^o)$	6

Table 2. The four $\{10\bar{1}1\}$-$\{10\bar{1}2\}$ double twin variant groups.

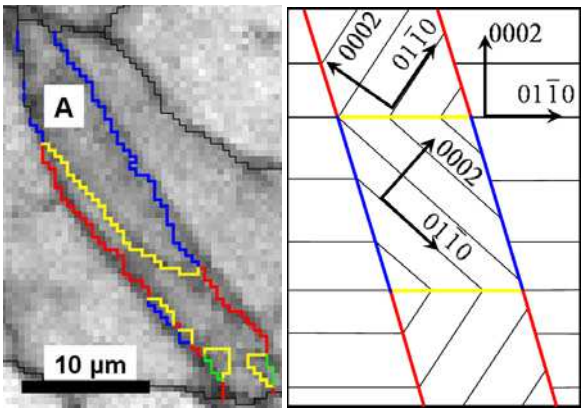

(a) (b)

Fig. 2. (a) EBSD map showing an S^A and an S^D secondary twin variants formed within a contraction twin, and (b) a schematic representation of an S^A secondary twin variant and the change of basal plane orientation. The $\{10\bar{1}1\}$ contraction twin boundaries are shown in red (56° $<1\bar{2}10>$ +/-5°), $\{10\bar{1}2\}$ extension in yellow (86° $<1\bar{2}10>$ +/-5°), the double twin boundaries associated with variant A (38° $<1\bar{2}10>$ +/-4°) in blue, and variant D (69.9° $<14\bar{7}\bar{7}3>$ +/-4°) in green. The tensile axis is vertical on this figure.

An example of secondary twins propagating within a contraction twin is displayed in Fig. 2 (a). The upper part of the primary twin has transformed into an S^A double twin while an S^D double twin has nucleated in the lower part. Since these secondary twins are *extension* twins, each double twin variant is delineated from the primary twin by an extension twin boundary (86° around $<1\bar{2}10>$). However, the boundaries that delineate the matrix and the double twin are the net result of two successive rotations and thus depend on the particular combination of the contraction and extension twin variants that is activated. The reorientation of the basal plane associated with the formation of an S^A double twin variant is illustrated in Fig. 2 (b)). The more favourable alignment of the basal slip plane (compared to the parent grain orientation) is shown, as well as the development of the secondary (extension) twin in the primary (contraction) twin interior.

4.2 Variant selection during primary and secondary twinning

A basal pole figure representation of the 6 primary twin and 36 double twin orientations that can form in a [0,0,0][2] orientated grain (in terms of Euler angles) is presented in Fig. 3. Each group of variants (S^A, S^B, S^C and S^D) is illustrated with a different symbol and a color code links each set of six secondary twin variants to its respective primary twin. The pole figure representation reveals the considerable potential for texture randomization as a single orientation may split into as many as 42 new orientations. Note that the S^A and S^B variants *decrease* the misorientation angle with respect to the matrix compared to that associated with the contraction twins. By contrast, the misorientations are *increased* when the S^C and S^D variants are activated.

The description of the variant selection associated with primary and secondary twinning is a laborious task: each grain is associated with 42 variants and each sample includes hundreds of grains. The characterization of these twins is however simplified when the *misorientations* rather than the orientations are considered. The rotation that links each twin (primary or secondary) to the parent orientation was thus measured from the EBSD scans performed on the deformed samples. The misorientations were obtained by considering the mean matrix grain and mean twin orientations. Each rotation was then applied to a perfect [0,0,0] orientation. The new orientations obtained correspond to the positions of the twins when the parent grain host is taken as the origin of the pole figure. In this way, the character of the variant selection is immediately evident when these orientations are superimposed on the ideal twin orientations in Fig. 3.

It can be seen that only four of the six possible primary twins are activated under the present strain path conditions. Such selection is associated with differences in the Schmid factors (SF's) of the variants: those selected were formed on the four systems with the highest SF's (Martin et al., 2010). Numerous secondary twins are clustered close to the four S^A and S^D locations associated with the four observed primary variants. Further selection occurs within the S^D group of variants since only four variants were detected (out of a possible eight associated with the four observed primary twin variants). By contrast, the S^B and S^C variants are almost never observed. The few twins situated close to these variants probably resulted from additional deformation-induced lattice rotations occurring within the S^A and S^D variants (Martin et al., 2010). The secondary twinning that took place was thus limited to the formation of only two of the four geometric configurations. The double twins only developed matrix misorientations of 37.5° or 69.9°. Since only four primary twins were activated, the 42 possible twin orientations were reduced to 12. Such variant selection is a major limitation to randomization of the crystallographic texture.

4.3 Recrystallization of contraction and double twins

Annealing of the twinned samples at 300 °C led to recrystallization of the twins. An example of an initial grain containing both recrystallized and unrecrystallized twins is displayed in Fig. 4. Here the local misorientation is specified by the colour as defined by the kernel average misorientation (KAM) approach. At a given point in the EBSD scan, the average misorientation of the point with respect to its immediate neighbors is calculated. The local misorientation is linked to the local lattice curvature; both these quantities are closely

[2] The reference frame is chosen so that the $< 10\bar{1}0 >$, $< \bar{1}2\bar{1}0 >$ and <0002> directions correspond to the x, y and z axes.

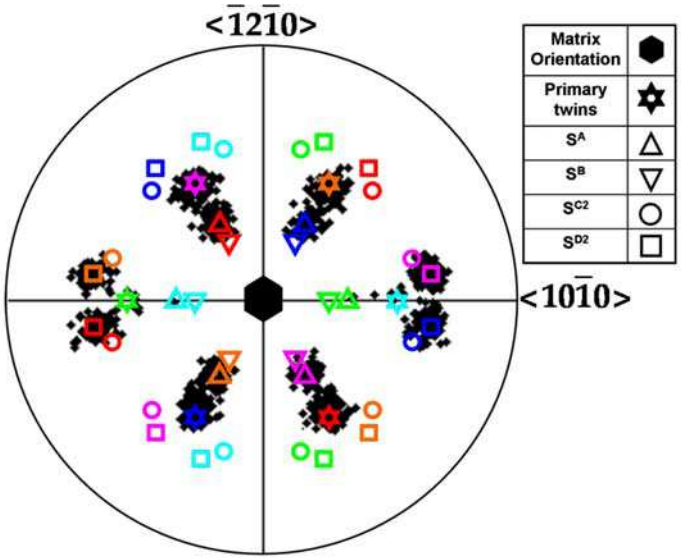

Fig. 3. {0002} pole figure of the measured primary and secondary twins (black dots) present in samples of AM30 and AZ31 deformed to 0.15 strain. The orientations were obtained by applying the rotation associated with each twin to a [0,0,0] orientation (black hexagon in the centre of the pole figure). The ideal (predicted) orientations of the six primary (colored stars) and 36 secondary twins are also displayed. The color code relates the secondary twin variants (circles, squares and triangles) to their respective primary twin variants (stars).

related to the stored energy and dislocation density. The twins have higher KAM values than the matrix grains. This is because the twins are narrow and more favorably oriented for basal slip, so that dislocation pile-up occurs more readily. Some unindexed twin networks are even revealed by their high KAM values (see the red arrows in Fig. 4). The driving forces for nucleation and growth are thus limited essentially to the neighborhoods of the twins. Indeed, the shapes of the new grains (identified with black arrows) follow those of their parent twins, so that the original coarse grains were not consumed by the recrystallizing grains even after 60 minutes of annealing. They were instead subdivided by the lamellae of the elongated new grains visible in Fig. 4. The widths of the recrystallized lamellae varied within the annealed samples. This is due to the uneven distribution of twins in the deformed samples. When twins are closely spaced, nucleus growth can occur within a larger region of stored energy leading to larger new grains (Martin et al., 2009).

The formation of a *secondary* twin produces strain incompatibilities within the parent grain (Martin et al., 2010). Such regions of strain concentration are preferred sites for nucleation. Moreover, the secondary twins and their matrix grains are not separated by special (CSL) boundaries, while the contraction twin boundaries have stable configurations and are generally considered to be immobile (Li et al., 2009). The double twin boundaries are thus more mobile and nucleation is initiated more readily in their vicinity. This interpretation is supported by Fig. 5, which shows that ~70% of the secondary twin boundaries have already lost their character after 30 minutes of annealing at 300 ^{o}C; by contrast, the contraction twins only *begin* to vanish after 30 minutes.

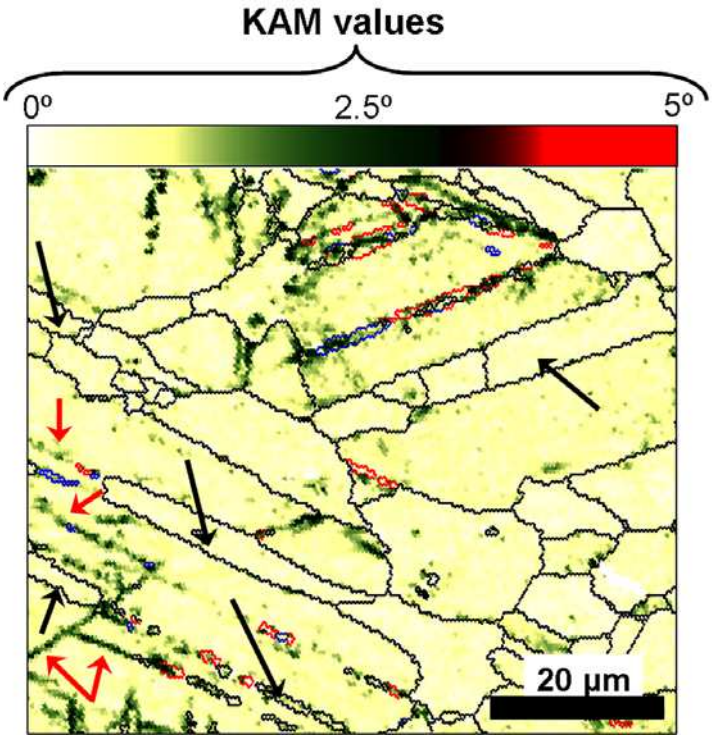

Fig. 4. EBSD map of a twinned sample annealed for 30 minutes at 300 ºC. KAM coloring is used as the background while the different types of twins are highlighted using the color scheme of Fig. 2 (a).

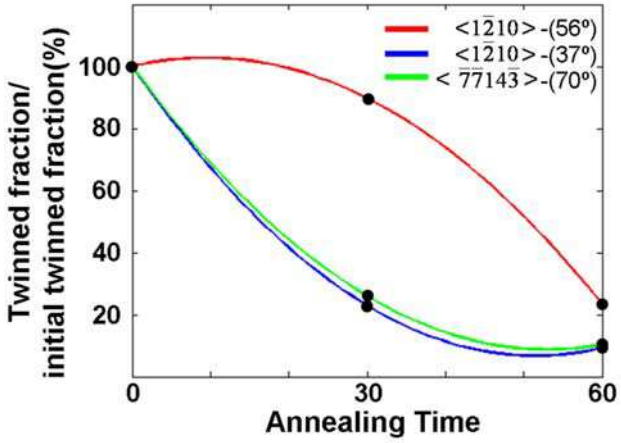

Fig. 5. Evolution of the twin boundary fractions in the magnesium AZ31 during annealing at 300 ºC.

4.4 Crystallographic orientations associated with annealing twins

From the above discussion, it can be concluded that annealing twinned samples cannot lead to significant texture changes since the un-twinned matrix grains are not consumed by growth of the twin-based nuclei. Indeed, the macrotextures of as-deformed samples and annealed ones display similar intensities, see Fig. 6. In special cases, nucleation can occur at the intersection of two S^A double twins when they share a common rotation axis (the blue and orange variants in Fig. 3, for example). Even though these nuclei grew during subsequent annealing, their new orientations are related to those of their parent grains by rotations about an axis close to the <0001> (Yi et al., 2009a). Because of this, they contribute to the persistence of the basal texture. Nevertheless, a slight shift of the major texture component is observed when the deformation texture is compared to the annealing texture, see Fig. 6. The intensity of the TD component is decreased by annealing, while that of the RD component is strengthened after 60 minutes of annealing.

The orientation changes associated with twin recrystallization are illustrated in Fig. 7. As in Fig. 3, the rotations that link recrystallized grains to their adjoining matrix grains were deduced from the EBSD data in the AZ31 and AM30. The rotations were then applied to a perfect [0,0,0] orientation (centre of the pole figure). Thus, the centre of the pole figure represents the matrix grain for each recrystallized grain. The 4 primary twin variants observed in the deformation microstructure prior to annealing (see Fig. 3) as well as the 8 (4 S^A and 4 S^D) secondary variants are superimposed here. They illustrate the 12 possible orientations within which the recrystallized grains are able to nucleate. The evolution of the recrystallized twin orientations from the as-received to the annealing material can thus be followed in Fig. 7.

Even though most of the twin boundaries lose their character during annealing, the new grains in Fig. 7 can still be associated in an approximate way with their respective parent twins. The recrystallized grains are, for the most part, restricted to two regions. In the first, recrystallization of the four S^D twin variants induces a spread around these orientations. This event corresponds exactly to the modification of the RD component observed in Fig. 6. The second group of new grains originated from the four S^A twin variants; their c-axes are rotated *towards* the matrix orientation (the centre of the pole figure in Fig. 7). The rotation axes associated with these grains are inclined with respect to the c-axis by about 30° to 60° (Martin et al., 2009). Thus, they do not correspond to the above description of nucleation at S^A double twin intersections.

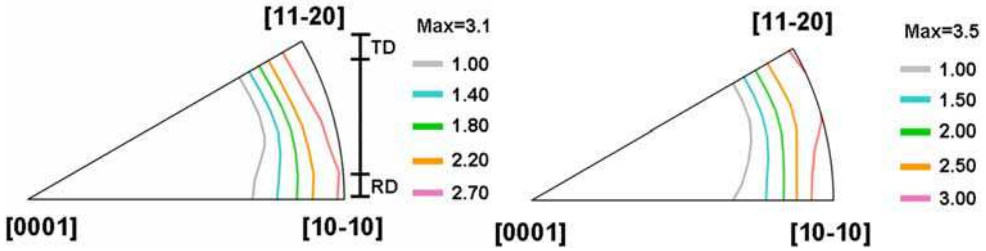

Fig. 6. Inverse pole figures displaying the orientations of the extrusion direction (ED) in the hexagonal crystal reference frame of the AZ31 (a) after 15% tensile strain and (b) after 1 hour annealing at 300 °C.

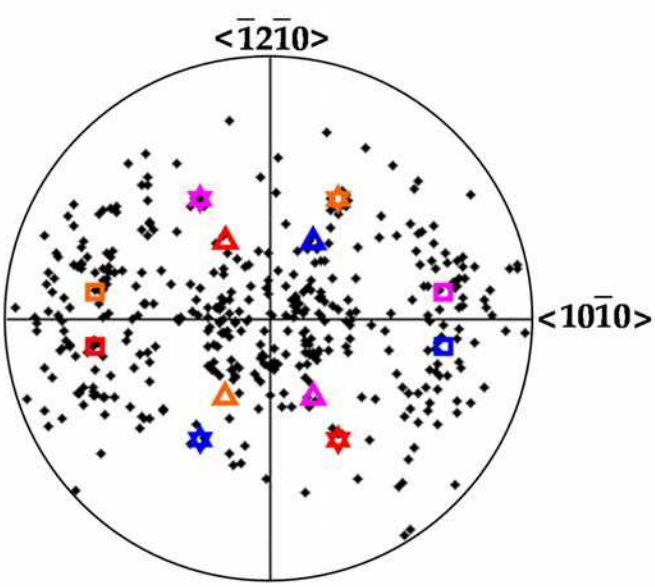

Fig. 7. Basal pole figure displaying the recrystallized grains (black dots) present in AM30 and AZ31 samples deformed to 0.15 strain and annealed for 1 hour. These orientations were deduced by employing the rotation associated with each grain with respect to the [0,0,0] orientation (center of the pole figure). The ideal (predicted) orientations of selected primary (six-pointed stars) and secondary (squares and triangles) twin variants are also plotted using the nomenclature of Fig. 3.

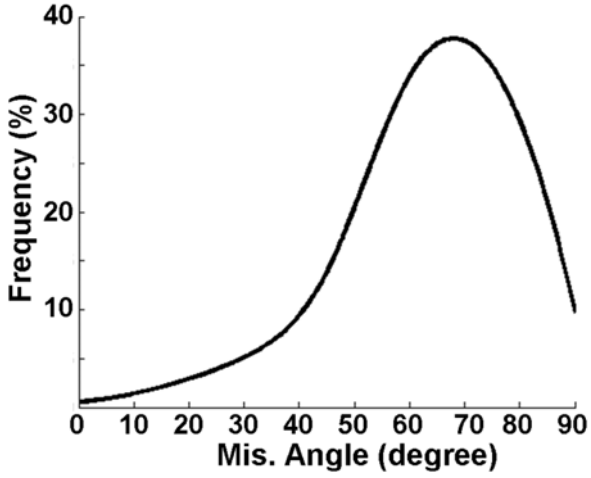

Fig. 8. Distribution of the misorientation angles between recrystallized grains and their primary twin hosts.

The misorientation distribution associated with the new grains (with respect to their primary twin hosts) is illustrated in Fig. 8. These misorientations were measured in partially recrystallized twins in the samples that were annealed for 30 minutes. The high intensity peak at ~70° reveals that the orientations of the recrystallized grains are closer to those of the secondary, rather than of the primary, twins. Because the secondary twins are of the extension type, they always have misorientation angles of 86° with respect to their primary twin hosts. There are few grains with orientations similar to the primary twin variants (four-pointed stars in Fig. 7); they have misorientations close to 0° in Fig. 8. This is because the nucleation rate is much higher in the vicinity of the double twins while growth is facilitated within the primary twins. As a result, contraction twins are more likely to vanish during growth of the double twin nuclei rather than to provide recrystallization nuclei.

5. Continuous and discontinuous recrystallization

As the Zener-Hollomon parameter of the deformation is decreased, the ease of cross-slip increases, (Couret & Caillard, 1985) and the accumulation and rearrangement of dislocations leads to the formation of numerous low-angle boundaries (LABs). Subsequent continuous rotation of the new substructures results in a progressive increase in misorientation and in the gradual appearance of more and more high angle boundaries (HABs) (Ion et al., 1982; Galiyev et al., 2001; Tan & Tan, 2003). This process is generally referred to as continuous dynamic recrystallization (cDRX) or extended recovery. Moreover, when the activation energy of plastic flow approaches that for volume self-diffusion (~135 kJ mol^{-1} in Mg (Frost & Ashby, 1982)), the controlling deformation mechanism becomes the climb of basal dislocations (Galiyev et al., 2001; Barnett, 2003). DRX nucleation by the bulging of initial grain boundaries (also referred to as discontinuous dynamic recrystallization (dDRX)) is also frequently reported under such deformation conditions (Sitdikov & Kaibyshev, 2001; Guo et al., 2005; Martin et al., 2008).

The cDRX and dDRX mechanisms were investigated in the present magnesium alloys on samples deformed at a high temperature (350 °C) and a low strain rate (0.001 s^{-1}) in order to promote the occurrence of recovery and diffusion. The specimens were compressed rather than pulled in tension to facilitate the cooling of the samples and to preserve the deformation microstructure. Because the compressive stress was applied along the ED (i.e. the $< 1\bar{2}10 >$ and $< 01\bar{1}0 >$ directions in the TD and RD components, respectively), extensive deviator tensile stresses were induced along the c -axes. Under such conditions, extension twinning would normally be favored. However, as straining was carried out below the critical value of the Zener–Hollomon parameter for the activation of twinning (~ 7×10^{12} s^{-1}), i.e. at stresses below that required to activate twinning, the deformation was essentially accommodated by slip.

5.1 Microbands and kink bands

In the early stages of high temperature deformation, magnesium grains are fragmented by geometrically necessary boundaries (GNBs). These boundaries separate microbands (MBs) of material with distinctly different orientations. Examples of the MBs and GNBs present in magnesium alloy AM30 deformed to a true strain of 0.05 at 350 °C are displayed in Fig. 9(a). The boundaries are essentially straight, are oriented perpendicular to the compression axis, and traverse into the grain interior.

Such boundaries are also referred to as kink boundaries (Yang et al., 2009) as they are occasionally present in closely spaced, parallel pairs. In such cases, there is a double change

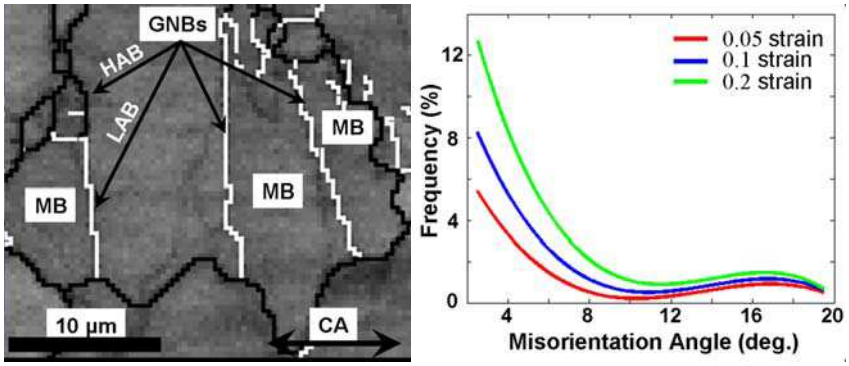

(a) (b)

Fig. 9. (a) EBSD map illustrating the geometrically necessary boundaries (highlighted by the black arrows) that delineate microbands. The low-angle boundaries ($5^o<\omega<15^o$) are shown in white and the high-angle boundaries ($\omega \geq 15^o$) in black. (b) Misorientation frequencies of the boundaries developed during the hot compression of magnesium AM30.

of orientation, which is generally self-compensating. Nevertheless, the rotation characteristics associated with the individual boundaries pertaining to these two types of bands are similar, so that the above discussion applies to kink bands (KBs) as well as MB boundaries.

The formation of MBs and KBs is attributed to the mechanism of dynamic recovery. Indeed, their concentration increases rapidly with strain, as shown indirectly in Fig. 9(b). The misorientations of the GNBs and kink boundaries increase progressively with strain. However, the rate of increase is significantly lower when the boundaries take on misorientation angles above 8^o.

The formation of MBs and KBs is depicted schematically in Fig. 10. In the present work, the planes of these bands (GNBs and kink boundaries) were essentially perpendicular to the compression axis; thus they are not crystallographic. Even though the prismatic and <c+a> slip systems are more favorably oriented for glide under the loading conditions of Fig. 10, MBs and KBs are nevertheless formed by the accumulation and rearrangement of *basal* dislocations (Martin & Jonas, 2010). Even a small inclination of the basal plane with respect to the compression axis is enough to promote basal glide because of the very low CRSS for this type of slip. In the experiments carried out to strains of 0.05 described here, the grains that contained MBs had higher Schmid factors for basal slip (SF =0.15) than the grains in which these bands were absent (SF =0.07). Moreover, according to Frank's formula (Hirth & Lothe, 1968), the polygonization of basal edge dislocations leads to rotation axes that lie in the basal plane and are thus perpendicular to the compression axis. In this way, the c-axes are gradually rotated towards the compression axis, moving the basal slip systems away from the hard slip towards the softer slip directions (Martin & Jonas, 2010).

5.2 Continuous dynamic recrystallization

During the hot deformation of magnesium, substructures ($\omega < 15^o$) gradually form in the grain interiors. The misorientation and number of such boundaries increase rapidly with strain, resulting in the in-situ evolution of new grains. The progressive increase in the boundary misorientation during deformation has been frequently reported in the literature and is referred to as continuous DRX (Kaibyshev & Sitdikov, 1996; Yang et al., 2003).

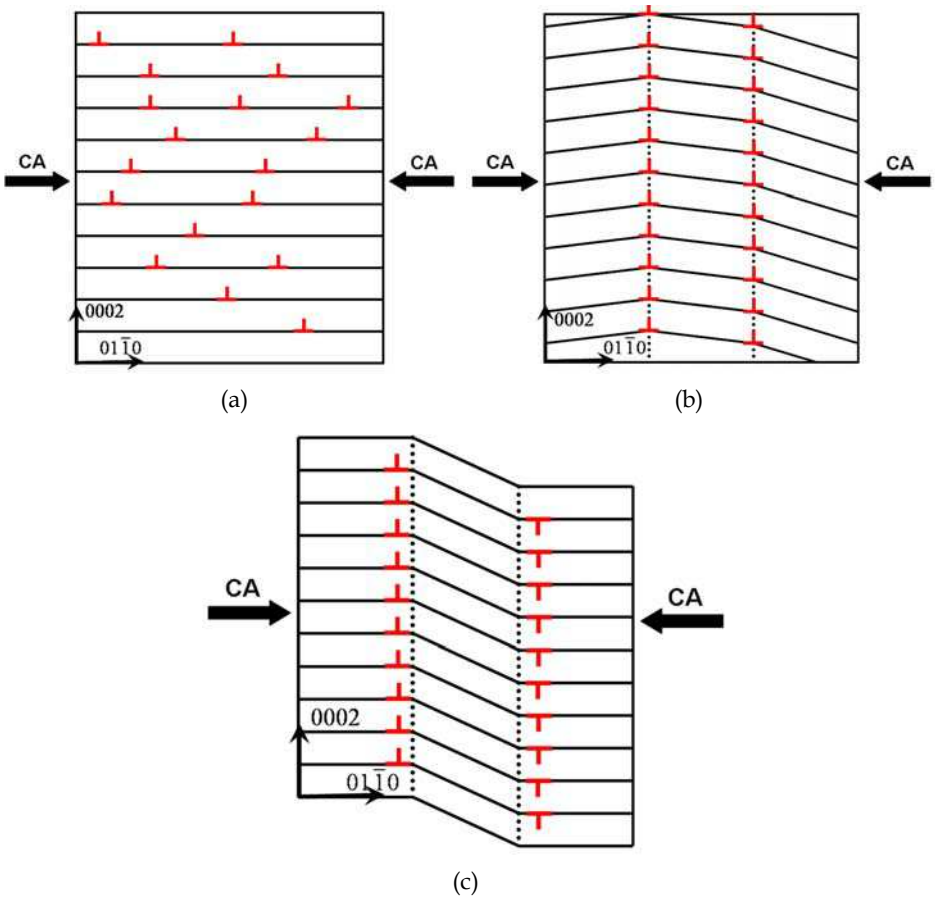

Fig. 10. A schematic representation of the formation of microbands and kink bands, their associated boundaries, and the associated changes in basal plane orientation. (a) An RD grain deformed in compression, (b) the microbands originate from the rearrangement of basal dislocations (shown in red), and (c) when two dislocation walls are composed of basal dislocations of opposite sign, the rotations are self-compensating and a kink band forms. The dotted lines correspond to the geometrically necessary boundaries and the kink boundaries in (b) and (c), respectively.

The evolution of such dislocation networks has been studied in detail. (Tan & Tan, 2003). However, TEM–based *microtexture* investigations do not generally provide statistically relevant analyses because of the very small volumes examined in a single specimen; they also require laborious specimen preparation. These limitations can be overcome by using microtexture analysis based on the EBSD technique. The very high measurement speed that can be achieved (currently more than 300 measurements per second) contributes to their effectiveness. However, the angular resolution is limited, so that the boundary rotation axes cannot be determined with accuracy when the misorientation is less than 5° (Prior, 1999; Wilkinson, 2001).

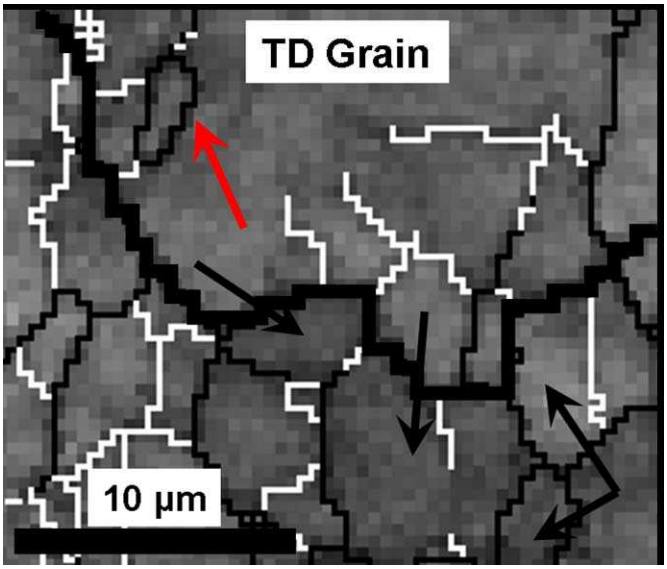

Fig. 11. EBSD map of a sample deformed to a strain of 0.2 at 350 °C. The sub-boundaries ($5^o<\omega<15^o$) are delineated by thin white lines; the new grains ($\omega \geq 15^o$) are outlined in black (see the red and black arrows). The initial grain boundary is shown as a thick black line.

The new grains that developed within the deformation substructure are illustrated in Fig. 11. These grains do not differ in size from the surrounding subgrains. They began their existence as subgrains entirely enclosed by LAB's. On becoming grains, they are enclosed by HAB's. In order to demonstrate that cDRX grains are produced by dislocation rearrangement, the c-axis orientations associated with matrix grains were compared with these of new grains. For this purpose, the angle α between the c-axis of a given crystallite and the compression axis was derived as follows:

$$\alpha = \arccos\left([\, g^{-1} <001>] \bullet <CA>\right) \tag{5}$$

Here **g** is the orientation matrix of the crystallite given by the triplet of Euler angles provided by the EBSD scan and <001> is the c-axis direction as expressed in an orthogonal reference frame. Then, the difference between the c-axis orientations of crystallites A and B with respect to the CA is obtained from:

$$\alpha_A - \alpha_B \tag{6}$$

where α_A and α_B are the angles between the c-axis and the CA associated with crystallites A and B, respectively. In this case, the A crystallite refers to the matrix, while the B crystallite refers to the microstructure feature of interest (i.e. the MB, KB, subgrain or new grain). Finally, these differences are normalized with respect to the rotation angle ω calculated from Eqs. 1 and 2 as follows:

$$\theta = \frac{\alpha_A - \alpha_B}{\omega} \tag{7}$$

According to Eq. 7, a boundary will have a θ value of one if the c-axis rotation towards the CA associated with it is equal to its misorientation angle ω. Positive values of θ describe c-axis rotations toward the CA, while negative values are associated with c-axis movements away from the CA. Finally, θ is zero under two conditions: i) if only a rotation about the c-axis is involved; and ii) if the c-axis is rotated around an axis that is parallel to CA.
Fig. 12 (a) shows that MBs and KBs are largely associated with a θ value of one, meaning that the c-axes are rotated towards the stress direction when these features are formed. This

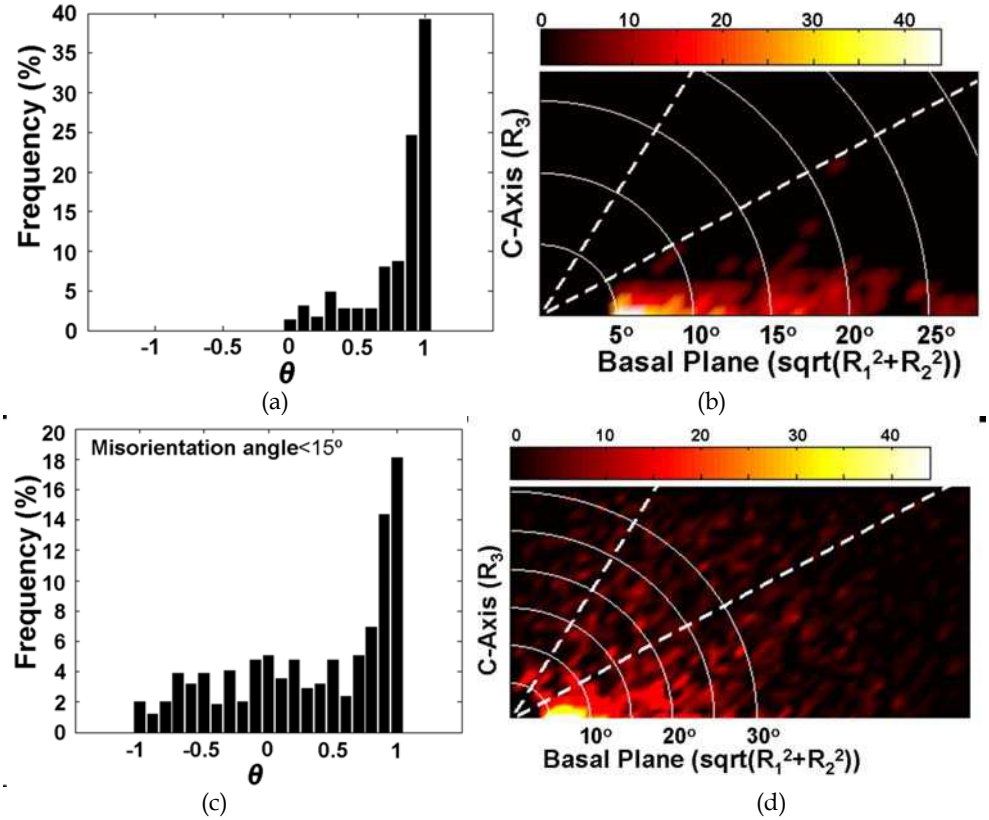

Fig. 12. c-axis displacements towards the CA direction attributable to the formation of (a) microbands and kinkbands and (c) subgrains. Side views of the reduced zones[3] displaying the rotations associated with (b) MBs and KBs and (d) new grains. The two dashed white lines represent vectors that are inclined at 30° and 60° to the c-axis and the white quarter circles identify the misorientation angles associated with the Rodrigues-Frank (RF) vectors.

[3] These side views of Rodrigues-Frank space are displayed here by plotting the R_3 (c-axis) value as a function of the projected length of the R-F vector on the basal plane ($\sqrt{R_1^2 + R_2^2}$). In this way, the inclinations of the RF vectors with respect to the c-axis are immediately evident; the lengths of the vectors are also preserved (see (Martin & Jonas (2010))).

type of rotation corresponds to the accumulation of basal dislocations. The inverse pole figures displayed in Fig. 1 show that the c-axes are initially aligned perpendicular to the compression axis. During the discussion of twinning presented above, it was stated that such a texture is unstable with respect to the compressive loading. The activation and especially the accumulation of basal dislocations thus lead invariably to rotations of the c-axes towards the contraction direction (the stable final orientation).

Further evidence is provided when the axis-angle pairs describing the MBs-KBs are considered. In Fig. 12 (b), the rotations are expressed in the form of Rodrigues-Frank vectors. Since MBs-KBs result from the progressive accumulation of basal dislocations, their rotations (Fig. 12 (b)) lie essentially in the basal plane and take on low to high angles in magnitude.

The characteristics of the rotations associated with subgrain formation are displayed in Fig. 12 (c). Here, the θ distribution is more broadly based than in Fig. 12(a), although it does exhibit a peak close to θ=1. These rotations also exhibit a strong intensity peak near 5^o (Fig. 12(d)), where the axes again lie mostly near the basal plane. The formation of subgrains thus also involves the progressive accumulation of basal dislocations. However, as the misorientation angles increase (see the range from $10^o \leq \omega \leq 20^o$ in Fig. 12(d)), the inclinations of the rotation axes with respect to the basal plane increase.

According to Frank's formula, this change is consistent with the view that prismatic and/or <c + a> dislocations are incorporated into the sub-boundaries as they gradually take on a high angle character. The activation of non-basal dislocations is required in the vicinities of the initial boundaries in order to accommodate the large plastic incompatibility stresses (Koike et al., 2003). The differences between the two distributions therefore arise because the cDRX grains considered here were formed essentially near the initial grain boundaries while the MBs-KBs developed in the grain interiors.

5.3 Discontinuous dynamic recrystallization

As the misorientation angles increase in Fig. 12(b), the RF vectors associated with the MBs and KBs remain close to the basal plane and their misorientations rarely exceed 20^o. This is because the formation of these boundaries, even those of high misorientation, continues to involve the pile-up of basal dislocations. Conversely, the differences in the distribution of the RF vectors associated with the new grains ($\omega > 20^o$) in Fig. 12(d) reveal that a second mechanism is involved in the formation of new DRX grains. In the first place, the RF vectors are more evenly distributed. Furthermore, there are many new grains with misorientation angles higher than 20^o. These two observations are inconsistent with the view that these ($\omega > 20^o$) grains were formed by cDRX.

This can be seen more clearly by examining the RF vectors that describe the initial microstructure, as illustrated in Fig. 13(a). These were measured in the as-received AM30 tubes. This distribution is somewhat similar to that associated with the new ($\omega > 20^o$) grains displayed in Fig. 12(d); in the two cases, 63% ±3% of the RF vectors are within 30^o of the basal plane, while the regions near the c-axis are clearly not favoured (8% ±1%). The similarity can be attributed to the formation of the new grains by the bulging of the pre-existing grain boundaries. In this way, their boundary misorientation characteristics reproduce those of their parent grains.

Of course the mother grains of bulged new grains cannot be identified with certainty. If bulging is initiated in a grain right above or below the plane of section, the mother grain is

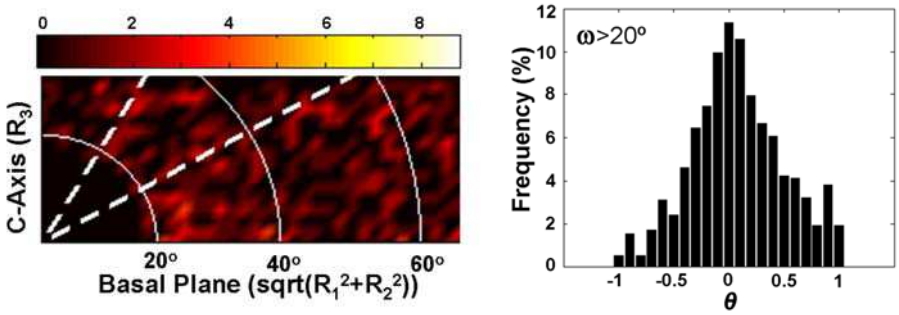

(a) (b)

Fig. 13. (a) Side view of the reduced zone displaying the misorientations associated with the initial grain boundaries. (b) c-axis displacements with respect to the CA direction attributable to the formation of new grains (delineated by HAB's).

not on the polishing plane. This is an inherent weakness of 2D metallography. In Fig. 11, the grain highlighted by the red arrow was considered to be a cDRX grain and the surrounding TD grain to be the mother grain. However, the new grain could have formed by the bulging of a grain right above or below the plane of the image, i.e. by a dDRX rather than a cDRX process. In this case, the HAB highlighted by the red arrow could have migrated from the initial grain into the TD grain. In such a case, the rotation characteristics would correspond to those of the *initial* grain boundaries rather than to those of the boundaries produced by the accumulation of basal dislocations.

A characteristic feature of the discontinuous mechanism is that the new grains have orientations that are similar to those of the old grains out of which they have grown. The boundaries of new grains have misorientation angles that generally exceeded 20º. It can be seen from Fig. 13 (b) that, in such a case, most of the c-axes rotate about axes that are approximately parallel to the compression axis (i.e. much of the distribution falls within $-0.25 < \theta < +0.25$ and is centered exactly on $\theta = 0$). In this way, the new grains have orientations close to those of the initial grains. Thus, more generally, new grains within the RD-TD fibre tend to grow within the other RD-TD fibre grains, as long as the latter are of different orientation. As a consequence, the main features of the initial RD-TD texture are retained during discontinuous dynamic recrystallization, even if the maximum intensity is somewhat reduced (Martin & Jonas, 2010).

The driving force for bulging is usually assumed to be the difference in dislocation density on opposite sides of the grain boundary. In a material with a well-recovered substructure, the low dislocation density region may be a large single subgrain (Humphreys & Hatherly, 2004). A bulge of this type, enclosed by a well defined subgrain with no detectable substructure within it, is illustrated in Fig. 14(a). Other subgrains may rotate during deformation into orientations that differ slightly from those of their parents (Martin & Jonas, 2010). Examples of bulge grains of somewhat different orientations, and therefore delineated by HABs, are displayed in Fig. 14(b).

In many metals, bulging is particularly important when deforming to low strains. In aluminum, for example, this mechanism is replaced when the rolling reduction exceeds 40% (Beck & Sperry, 1950). As the present work was restricted to low strain deformation, no conclusions can be drawn about the possible role of bulging in highly deformed magnesium alloys.

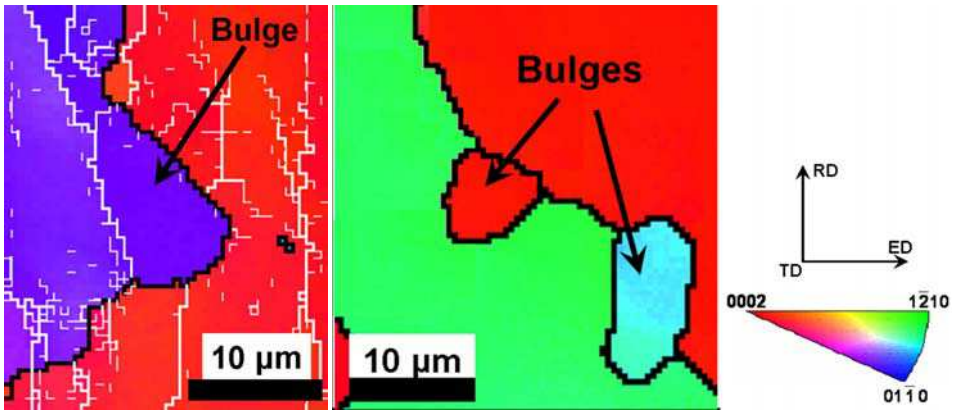

(a) (b)

Fig. 14. Inverse pole figure (IPF) maps of an AM30 sample deformed to 0.2 strain; three examples of bulge nucleation are shown. The low-angle boundaries ($2^o<\omega<15^o$) are shown in white and the high-angle boundaries ($\omega \geq 15^o$) in black. The IPF color triangle indicates the orientation of the TD axis in the hexagonal crystal reference system.

6. Conclusions

The recrystallization of magnesium is a fairly complex topic, essentially because the deformation of magnesium involves several different mechanisms. Furthermore, the subsequent occurrence of recrystallization also involves several mechanisms, which may occur simultaneously. Mesoscale (i.e. grain scale) investigations are thus especially suitable for the exploration of such phenomena. The crystallographic characterization of the recrystallization phenomena described here has led to the clarification of the contributions of the different nucleation mechanisms to texture evolution. Moreover, by considering the deformation structure within which the new grains nucleate, it has been possible to gain some insights into the nucleation mechanisms themselves. The results described above have led to the following conclusions.

1. Strong variant selection takes place during the formation of primary and secondary twins. In the first case, the primary (contraction) twin orientations that are activated depend on the processing conditions. In the present case, these were limited to four out of six possible variants. It has been shown elsewhere (Martin et al., 2010) that secondary (extension) twins that require relatively easy accommodation strains tend to form. This is why only 18 out of 36 possible secondary twin variants can be activated in the general case. These all belong to the S^A and S^D variant categories (misorientations of 37.5^o and 69.9^o, respectively, with respect to the parent grain).
2. Double twins recrystallize more rapidly than primary twins during annealing. The new grains do not generate significant rotations (texture changes), so that the new orientations remain similar to those of the secondary twins. Recrystallization of the four S^D twin variants induces a spread around these orientations. On the other hand, recrystallization of the S^A twin variants rotates the c-axes towards the parent grain orientations, so that they contribute to the persistence of the initial texture.

3. The double twin nuclei tend to grow solely within the primary twins rather than spreading into the parent grains. This is because the primary twins are favorably orientated for basal slip, so that dislocation pile-up occurs more extensively within them. The driving forces for growth are thus larger within the twin lamella than within the parent grains. In this way, the primary twins do not contribute significantly to texture change since these twins are essentially consumed during growth of the secondary twin nuclei. They do not themselves provide recrystallization (and therefore new orientation) nuclei.
4. When the deformation temperature is increased sufficiently to allow significant recovery to take place, microbands and kink bands form by the accumulation and rearrangement of *basal* dislocations. They thus contribute to the formation of the basal (stable) end texture. These bands form in the early stages of high temperature deformation and lead to the formation of new grains with relatively low misorientations with respect to the parent grains. This is considered here to involve the continuous dynamic recrystallization mechanism.
5. New grains also form in magnesium due to the migration of the pre-existing grain boundaries. This is referred to here as discontinuous DRX or dDRX. The driving force for bulging arises from dislocation density and substructure size differences across the initial boundaries. These new "bulge" grains are initially enclosed by low angle boundaries that continuously increase in misorientation to become high angle boundaries. Nevertheless, the dDRX grains can still be differentiated from the cDRX grains. The former grains have orientations that are similar to those of the initial grains out of which they have grown. The formation of the basal texture is thus somewhat retarded when dDRX is taking place. By contrast, the cDRX grains essentially rotate the c-axes towards the basal end texture.

7. References

Backx, P.; Barnett, M. R. & Kestens, L. (2004). Texture changes during uniaxial compression of Mg-3Al-1Zn. *Materials Science Forum*, 467-470, 6.

Barnett, M. R. (2001). Influence of deformation conditions and texture on the high temperature flow stress of magnesium AZ31. *Journal of Light Metals* 1, 11.

Barnett, M. R. (2003). A Taylor model based description of the proof stress of magnesium AZ31 during hot working. *Metallurgical and Materials Transactions A*, 34, 8.

Barnett, M. R. (2007). Twinning and the ductility of magnesium alloys. Part II. "Contraction" twins. *Materials Science and Engineering A*, 464, 1-2, 8.

Beausir, B.; Suwas, S.; Toth, L.; Neale, K. W. & Fundenberger, J. J. (2007). Analysis of texture evolution in magnesium during equal channel angular extrusion. *Acta Materialia*, 56, 2, 15.

Beck, P. A. & Sperry, P. R. (1950). Strain induced grain boundary migration in high purity aluminum. *Journal of Applied Physics*, 221, 2, 3.

Bunge, H. J. (1982). *Texture Analysis in Material Science*, Butterworths, London

Couret, A. & Caillard, D. (1985). An in situ study of prismatic glide in magnesium - I: the rate controlling mechanism. *Acta Metallurgica*, 33, 8, 8.

del Valle, J. A.; Pérez-Prado, M. T. & Ruano, O. A. (2005). Deformation mechanisms responsible for the high ductility in a Mg AZ31 alloy analyzed by electron backscattered diffraction. *Metallurgical and Materials Transactions A* 36A, 12.

Engler, O. & Randle, V. (2010). *Introduction to Texture Analysis: Macrotexture, Microtexture & Orientation Mapping*, Gordon and Breach Science, New York

Frank, F. C. (1988). Orientation mapping. *Metallurgical Transactions A*, 19, 3, 6.

Frost, H. J. & Ashby, M. F. (1982). *Deformation-Mechanism Maps*, Pergamon Press, Oxford

Galiyev, A.; Kaibyshev, R. & Gottstein, G. (2001). Correlation of plastic deformation and dynamic recrystallization in magnesium alloy ZK60. *Acta Materialia*, 49, 8.

Godet, S.; Jiang, L.; Luo, A. A. & Jonas, J. J. (2006). Use of Schmid factors to select extension twin variants in extruded magnesium alloy tubes. *Scripta Materialia*, 55, 11, 4.

Gottstein, G. & Al Samman, T. (2005). Texture development in pure Mg and Mg alloy AZ31. *Materials Science Forum*, 495-497, PART 1, 10.

Guo, Q.; Yan, H. G.; Zhang, H.; Chen, Z. H. & Wang, Z. F. (2005). Behavior of AZ31 magnesium alloy during compression at elevated temperature. *Materials Science and technology*, 21, 11, 6.

Heinz, A. & Neumann, P. (1991). Representation of orientation and disorientation data for cubic, hexagonal, tetragonal and orthorhombic crystals. *Acta Crystallographica*, A47, 10.

Hirth, J. P. & Lothe, J. (1968). *Theory of Dislocations*, McGraw-Hill, New York

Humphreys, F. J. & Hatherly, M. (2004). *Recrystallization and Related Annealing Phenomena*, Elsevier, Oxford

Ion, S. E.; Humphreys, F. J. & White, S. H. (1982). Dynamic recrystallisation and the development of microstructure during the high temperature deformation of magnesium. *Acta Metallurgica*, 30, 11.

Jäger, A.; Lukác, P.; Gärtnerová, V.; Haloda, J. & Dopita, M. (2006). Influence of annealing on the microstructure of commercial Mg alloy AZ31 after mechanical forming. *Materials Science and Engineering A*, 432, 1-2, 6.

Jiang, L.; Jonas, J. J.; Luo, A. A.; Sachdev, A. K. & Godet, S. (2006). Twinning-induced softening in polycrystalline AM30 Mg alloy at moderate temperatures. *Scripta Materialia*, 54, 5, 5.

Jiang, L.; Jonas, J. J.; Mishra, R. K.; Luo, A. A.; Sachdev, A. K. & Godet, S. (2007). Twinning and texture development in two Mg alloys subjected to loading along three different strain paths. *Acta Materialia*, 55, 12.

Kaibyshev, R. O. & Sitdikov, O. (1996). Bulging mechanism of dynamic recrystallization. *Proceedings of Third international conference on recrystallisation and related phenomena*.

Kleiner, S. & Uggowitzer, P. J. (2004). Mechanical anisotropy of extruded Mg–6% Al–1% Zn alloy. *Materials Science and Engineering A*, 379, 1-2, 6.

Kocks, U. F.; Tomé, C. N. & Wenk, H.-R. (1998). *Texture and Anisotropy : Preferred Orientation in Polycrystals and their Effect on Materials Properties*, Cambridge University Press, Cambridge

Koike, J.; Kobayashi, T.; Mukai, T.; Watanabe, H.; Suzuki, M.; Maruyama, K. & Higashi, K. (2003). The activity of non-basal slip systems and dynamic recovery at room temperature in fine-grained AZ31B magnesium alloys. *Acta Materialia*, 51, 6, 11.

Li, X.; Yang, P.; Wang, L.-N.; Meng, L. & Cui, F. (2009). Orientational analysis of static recrystallization at compression twins in a magnesium alloy AZ31. *Material Science and Engineering A*, 517, 10.

Martin, E.; Godet, S.; Jiang, L.; Elwazri, A.; Jacques, P. J. & Jonas, J. J. (2008). An EBSD study of the misorientations related to dynamic recrystallization in Mg AM30 deformed at high temperatures. *Proceedings of 15th International Conference on Textures of Materials*, Pittsburgh, PA, United States, American Ceramic Society, 577.

Martin, E.; Jiang, L.; Godet, S. & Jonas, J. J. (2009). The combined effect of static recrystallization and twinning on texture in magnesium alloys AM30 and AZ31. *International Journal of Materials Research*, 100, 8.

Martin, E. & Jonas, J. J. (2010). Evolution of Microstructure and Microtexture during the Hot Deformation of Mg -3% Al. *Acta Materialia*. *58,12, 15*.

Martin, E.; Capolungo, L.; Jiang, L. & Jonas, J. J. (2010). Variant selection during secondary twinning in Mg–3%Al. *Acta Materialia*. *58, 11, 15*.

Mason, J. K. & Schuh, C. A. (2008). Hyperspherical harmonics for the representation of crystallographic texture. *Acta materialia*, 56, 20, 15.

Myshlyaev, M. M.; McQueen, H. J.; Mwembela, A. & Konopleva, E. (2002). Twinning, dynamic recovery and recrystallization in hot worked Mg-Al-Zn alloy. *Materials Science and Engineering A*, 337, 13.

Polmear, I. J. (1995). *Light Alloys: Metallurgy of the Light Metals*, John Wiley and Sons, London

Prior, D. J. (1999). Problems in determining the misorientation axes, for small angular misorientations, using electron backscatter diffraction in the SEM. *Journal of Microscopy*, 195, 9.

Sitdikov, O. & Kaibyshev, R. (2001). Dynamic recrystallization in pure magnesium. *Materials Transactions*, 42, 6, 1928.

Tan, J. C. & Tan, M. J. (2003). Dynamic continuous recrystallization characteristics in two stage deformation of Mg-3Al-1Zn alloy sheet. *Materials Science and Engineering A*, 339, 9.

Wilkinson, A. J. (2001). A new method for determining small misorientation from electron back scatter diffraction patterns. *Scripta Materialia*, 44, 10, 7.

Yang, X.; Miura, H. & Sakai, T. (2003). Dynamic evolution of new grains in magnesium alloy AZ31 during hot deformation. *Materials Transactions*, 44, 1, 7.

Yang, X.; Ze-sheng, J.; Miura, H. & Sakai, T. (2009). Dynamic recrystallization and texture development during hot deformation of magnesium alloy AZ31. *Trans. Nonferrous Met. Soc. China*, 19, 4, 6.

Yi, S.; Schestakowb, I. & Zaefferer, S. (2009a). Twinning-related microstructural evolution during hot rolling and subsequent annealing of pure magnesium. *Materials Science and Engineering A*, 516, 7.

Yi, S.; Schestakow, I. & Zaefferer, S. & Brokmeier, H.-G. (2006). Mechanical behaviour and microstructural evolution of magnesium alloy AZ31 in tension at different temperatures. *Materials Science and Engineering A*, 424, 1-2, 7.

Yi, S. B.; Zaefferer, S. & Brokmeier, H.-G. (2009b). Twinning-related microstructural evolution during hot rolling and subsequent annealing of pure magnesium. *Materials Science & Engineering A*, 424, 1-2.

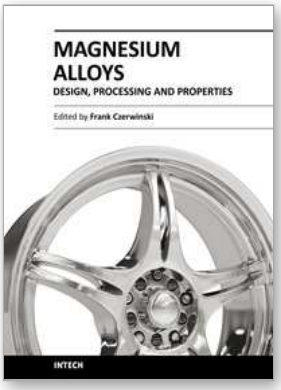

Magnesium Alloys - Design, Processing and Properties

Edited by Frank Czerwinski

ISBN 978-953-307-520-4
Hard cover, 526 pages
Publisher InTech
Published online 14, January, 2011
Published in print edition January, 2011

Scientists and engineers for decades searched to utilize magnesium, known of its low density, for light-weighting in many industrial sectors. This book provides a broad review of recent global developments in theory and practice of modern magnesium alloys. It covers fundamental aspects of alloy strengthening, recrystallization, details of microstructure and a unique role of grain refinement. The theory is linked with elements of alloy design and specific properties, including fatigue and creep resistance. Also technologies of alloy formation and processing, such as sheet rolling, semi-solid forming, welding and joining are considered. An opportunity of creation the metal matrix composite based on magnesium matrix is described along with carbon nanotubes as an effective reinforcement. A mixture of science and technology makes this book very useful for professionals from academia and industry.

How to reference

In order to correctly reference this scholarly work, feel free to copy and paste the following:

Étienne Martin, Raj K. Mishra and John J. Jonas (2011). Deformation Structures and Recrystallization in Magnesium Alloys, Magnesium Alloys - Design, Processing and Properties, Frank Czerwinski (Ed.), ISBN: 978-953-307-520-4, InTech, Available from: http://www.intechopen.com/books/magnesium-alloys-design-processing-and-properties/deformation-structures-and-recrystallization-in-magnesium-alloys

INTECH
open science | open minds

InTech Europe
University Campus STeP Ri
Slavka Krautzeka 83/A
51000 Rijeka, Croatia
Phone: +385 (51) 770 447
Fax: +385 (51) 686 166
www.intechopen.com

InTech China
Unit 405, Office Block, Hotel Equatorial Shanghai
No.65, Yan An Road (West), Shanghai, 200040, China
中国上海市延安西路65号上海国际贵都大饭店办公楼405单元
Phone: +86-21-62489820
Fax: +86-21-62489821